



Electrochemical generation of birnessite MnO₂ nanoflowers for intercalation of Mg²⁺ ions

Cheng Zhang^a, Xun Zhan^b, Talha Al-Zoubi^a, Yanling Ma^a, Pei-Chieh Shih^a, Fangfang Wang^a, Wenxiang Chen^{b,c}, Saran Pidaparthi^b, Ryan M. Stephens^f, Qian Chen^{b,c,d,e}, Jian-Min Zuo^{b,c}, Hong Yang^{a,c,d,*}

^a Department of Chemical and Biomolecular Engineering, University of Illinois at Urbana-Champaign, Urbana, IL 61801, United States

^b Department of Materials Science and Engineering, University of Illinois at Urbana-Champaign, Urbana, IL 61801, United States

^c Materials Research Laboratory, University of Illinois at Urbana-Champaign, Urbana, IL 61801, United States

^d Department of Chemistry, University of Illinois at Urbana-Champaign, Urbana, IL 61801, United States

^e Beckman Institute for Advanced Science and Technology, University of Illinois at Urbana-Champaign, Urbana, IL 61801, United States

^f Shell International Exploration & Production Inc., Houston, TX 77082, United States

ARTICLE INFO

Keywords:

Birnessite
MnO₂
In-situ conversion
Mg-ion insertion
Aqueous battery
Intercalation

ABSTRACT

Rechargeable multivalent ion battery such as Mg-ion battery is considered as a candidate for high-density battery technology because of its high volumetric capacity and low tendency to form dendrites. Development of cathode materials for Mg-ion batteries requires good understanding of the intercalation and adsorption processes of Mg²⁺ ions into and on the host materials. We observed recently that nanostructure is beneficial for the development of Mg²⁺ cathode materials with high capacity. In this work, we describe the preparation of flower-like three-dimensional (3D) nanostructures of birnessite MnO₂ through an electrochemical conversion reaction from γ -MnS. This 3D birnessite MnO₂ exhibited a total capacity of \sim 360 mAh/g in aqueous electrolyte for the initial cycle. We further characterized the insertion of Mg²⁺ ions in the atomic layers of MnO₂ nanoflowers using scanning transmission electron microscopy (STEM) technique, revealing the energy storage mechanism of Mg²⁺ ions in 3D, ion-accessible MnO₂ nanostructures.

1. Introduction

Multivalent ion batteries have attracted much attention in recent years as a next-generation technology for energy storage [1–15]. While lithium-ion batteries show impressive high performance, further improvement are needed to meet the energy density and low-cost requirement for the mobile and stationary energy storage applications [16–24]. In this context, Mg-ion battery is an alternative because of its high earth abundance (2.33×10^4 ppm for Mg vs. 20 ppm for Li), high volumetric capacity (3833 mAh/cm³ for Mg vs. 2046 mAh/cm³ for Li) and lack of dendrite formation when Mg metal is used as the anode [1–4]. Thus, there is a sustained research interest in Mg-ion batteries over the past decade despite of the challenges.

One main challenge is the development of high-capacity cathode materials due to the sluggish kinetics of divalent or other multivalent ions [3,25,26]. Chevrel phase Mo₆S₈ was identified to be a plausible cathode material for Mg-ion batteries [27], though its small discharge

voltage (1.1 V vs. Mg) and relatively low capacity (<100 mAh/g) limit its potential applications [28,29]. In recent years, researchers have studied other cathode materials for Mg-ion batteries including MnO₂ [30–44], spinel-phase Ti₂S₄ [45], olivine-phase MgFeSiO₄ [46], and layered V₂O₅ [47,48]. Among these candidates, MnO₂ exhibits high theoretical capacity (308 mAh/g), large discharge potential (\sim 2.8 V vs. Mg) and relatively low cost [1]. Different phases of MnO₂ have been studied for their charge storage performance, including hollandite α -MnO₂ [30], spinel λ -MnO₂ [31,32], and birnessite δ -MnO₂ [33–38,41, 49–51]. Birnessite MnO₂ is of interest for its layered structure with edge-sharing MnO₆ units [1,33]. It has been studied as supercapacitor material and explored as cathode material for multivalent ion batteries [33–38,52]. We reported recently that reducing the particle size of MnO₂ could greatly facilitate the intercalation of Mg²⁺ ions in the host materials [32]. This size-dependent enhancement in capacity suggests a new strategy for making active cathode materials by creating accessible nanostructures using layered MnO₂.

* Corresponding author at: Department of Chemical and Biomolecular Engineering, University of Illinois at Urbana-Champaign, Urbana, IL 61801, United States.
E-mail address: hy66@illinois.edu (H. Yang).

Here, we report a synthesis of flower-like nanostructures of birnessite MnO_2 through an unconventional, electrochemical conversion from $\gamma\text{-MnS}$ solid precursors. The electrochemical performances of birnessite MnO_2 nanoflowers as cathode materials for Mg-ion batteries were determined using a three-electrode system in an aqueous electrolyte [31, 32]. High-angle angular dark-field (HAADF) scanning transmission electron microscopy (STEM) and electron energy loss spectroscopy (EELS) provide direct evidence that Mg^{2+} ions intercalated into the layered structures of birnessite MnO_2 nanoflowers, aiding our understanding on the charge storage mechanism of multivalent ions in host materials.

2. Experimental

2.1. Materials

Manganese (II) acetate tetrahydrate ($\text{Mn}(\text{CH}_3\text{COO})_2 \cdot 0.4 \text{ H}_2\text{O}$, 99.99%, metals basis, Aldrich), polyvinylpyrrolidone (PVP, MW $\sim 29,000$, Aldrich), sulfur (S, >99.99%, Aldrich), ethylene glycol ($\text{C}_2\text{H}_6\text{O}_2$, Macron), polyvinylidene fluoride (PVDF, >99.5%, MTI Corporation), carbon black (Super P Conductive, 99 +%, metals basis, Alfa Aesar), activated carbon (MTI Corporation), magnesium nitrate hexahydrate ($\text{Mg}(\text{NO}_3)_2 \cdot 0.6 \text{ H}_2\text{O}$, 99%, Sigma-Aldrich), 1-methyl-2-pyrrolidinone (NMP, 99.5%, Sigma-Aldrich), carbon disulfide (CS_2 , 99.99%, Fisher Scientific), and ethanol (200 proof, Decon Labs, Inc) were used as received. The 304 stainless steel shim was purchased from 6304 to 1, Trinity Brand Industry. Silver-silver chloride reference electrode with porous Teflon tip was purchased from CH Instruments, Inc.

2.2. Synthesis of spherical $\gamma\text{-MnS}$

In a typical synthesis, 0.1575 g of $\text{Mn}(\text{CH}_3\text{COO})_2 \cdot 0.4 \text{ H}_2\text{O}$ (0.643 mmol), 0.3729 g of PVP (1.286×10^{-2} mmol) and 0.0206 g of S (0.643 mmol) were dissolved in 19.29 mL of ethylene glycol solvent in a home-made 45-mL Teflon liner. A uniform mixture was obtained by stirring vigorously for 1 h using a magnetic stirrer/hot plate (VWR, Cat. No. 97042–714). The Teflon liner was then sealed in a stainless-steel autoclave, heated at a ramping rate of $5^\circ\text{C}/\text{min}$ to 190°C and maintained at this temperature for 2 h in a box furnace (Thermo Fisher ScientificTM, Lindberg/Blue MTM). After the reaction, the autoclave was cooled to room temperature naturally. The resulting pink product (~ 30 mg) was collected and washed with 10 mL of DI water for three times, followed by centrifuging at 9000 rpm for 15 min (Beckman Coulter Inc., Allegra X-30 Series) until a clear supernatant was obtained. Then the sample was dried under vacuum at 60°C overnight to obtain the final product.

2.3. Electrochemical preparation of birnessite MnO_2 nanoflowers from $\gamma\text{-MnS}$

In a typical protocol, the synthesis was conducted in 50 mL glass cell using a standard three-electrode system, which was monitored and controlled by a potentiostat (CH Instruments 760E). Platinum wire was used as the counter electrode and Ag/AgCl as the reference electrode. The working electrode was prepared starting with mixing the spherical $\gamma\text{-MnS}$, carbon black (Super P), and PVDF at a mass ratio of 8:1:1 in a predetermined amount of 1-methyl-2-pyrrolidinone (NMP) solvent in an agate mortar. Typically, around 1 mL of NMP was used for making a slurry containing 0.1 g of spherical $\gamma\text{-MnS}$. This slurry was ground for 20–30 min in order to obtain a uniform mixture. The slurry was then cast on top of a stainless steel shim with a micrometer adjustable film applicator (film casting doctor blade, MTI) at a mass loading of ~ 1.5 mg/cm^2 . The stainless-steel shim with the cast slurry film was dried at 120°C overnight in a vacuum oven. A round disk of the stainless-steel shim (2 cm in diameter) was made by a disc cutter (MTI, MSK-T-06) and used as the working electrode. The carbon electrode was prepared using the same protocol as $\gamma\text{-MnS}$ by mixing activated carbon, carbon

black (Super P), and PVDF at a mass ratio of 8:1:1.

The electrochemical process for making birnessite MnO_2 nanoflowers started with galvanostatic charge and discharge cycles at a rate of 50 mA/g $\gamma\text{-MnS}$ cathode materials in the above three-electrode system using 40 mL of $\text{Mg}(\text{NO}_3)_2$ aqueous solution (1 M) as the electrolyte. The cycle range was set between -0.2 V and 1 V (vs. Ag/AgCl). The product formed after five cycles was collected on the working electrode upon the completion of the 5th charge. The obtained working electrode was rinsed with ~ 10 mL of DI water and dried at room temperature. The working electrode with the as-prepared materials was immersed in CS_2 for 2 h and then rinsed with 10 mL of ethanol for three times and dried at 80°C to remove the CS_2 solvent.

2.4. Electrochemical tests

Galvanostatic and cyclic voltammetry (CV) charge and discharge studies were conducted in the three-electrode cell as described above using the same amount of 1 M $\text{Mg}(\text{NO}_3)_2$ aqueous solution. Galvanostatic charge and discharge cycles were also in the voltage range between -0.2 V and 1 V (vs. Ag/AgCl) at a preset rate of 2 C (616 mA/g). The mass was calculated based on active materials on the working electrode after washing with CS_2 . The CV curves were measured in the voltage range from -0.6 – 1.2 V (vs. Ag/AgCl) at various scan rates. A conditioning cycle was carried out before the CV cycle was recorded for analysis.

Full cell tests were conducted in a beaker cell using a two-electrode system with 15 mL of $\text{Mg}(\text{NO}_3)_2$ aqueous solution (1 M) as the electrolyte. The cathode material served as the working electrode and the carbon electrode is the counter and reference electrode. Galvanostatic tests were performed in the voltage range between -0.8 V and 1 V (vs. carbon) at a rate of 1 C (308 mA/g). The Coulombic efficiency was calculated through dividing the charge capacity by discharge capacity.

2.5. Characterization

X-ray diffraction (XRD) of the powder samples was measured using a Rigaku Miniflex 600 diffractometer with $\text{Cu K}\alpha$ X-ray source ($\lambda = 1.54056 \text{ \AA}$). A typical run was between 10° and 80° 2θ at a scan rate of 0.04° 2θ per second. The powder was directly spread evenly on top of the sample holder. The XRD patterns for the samples on electrodes were collected on Bruker D8 Advance XRD system at a scan rate of 0.1° 2θ per second. The electrodes on the stainless foil were fixed on top of the sample holder with a small piece of clay. The XRD data was analyzed by using Jade 9.0 software (Materials Data, Inc).

High-resolution transmission electron microscopy (HRTEM) images were obtained using JEOL 2100 Cryo TEM with a LaB_6 emitter at 200 kV. For the preparation of TEM specimen, the formed powders were scratched off from the electrodes using a plastic spatula. The powder sample was then dispersed in about 1 mL of ethanol sonicated for 30 min to form a uniform dispersion. One drop of the dispersion was cast on a TEM grid and dried at room temperature to make the specimen.

Scanning electron microscopy (SEM) images were collected using a Hitachi S4700 microscope at an acceleration voltage of 10 kV. The specimen was prepared by spreading the powder samples ($\gamma\text{-MnS}$) or placing the electrodes on top of the sample holders using carbon tape. SEM energy-dispersive spectroscopy (EDS) was performed with analysis mode at a voltage of 20 kV. HAADF-STEM, STEM-EDS, and EELS were performed using a Themis Z analytical (S)TEM (Thermo Fisher) at a voltage of 300 kV. The preparation of the sample was the same as those specimen for HRTEM. HAADF-STEM images were collected at the beam current of ~ 20 pA, and HAADF detector semi-angles between 50 and 200 mrad. STEM-EDS mapping was obtained using a continuous scan mode with frame time of ~ 1 s for a total of around 30 min. EELS spectroscopy was acquired on a Gatan imaging filter (GIF Quantum 965) with an energy dispersion of 0.1 eV/channel. Energy Dispersive X-ray Fluorescence (EDXRF) was performed on a Shimadzu EDX-700

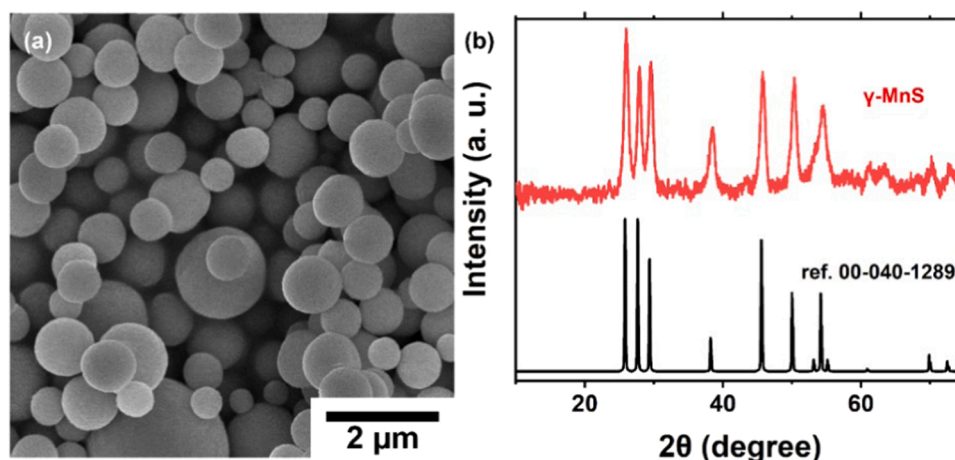


Fig. 1. (a) SEM image and (b) XRD pattern of γ -MnS spheres.

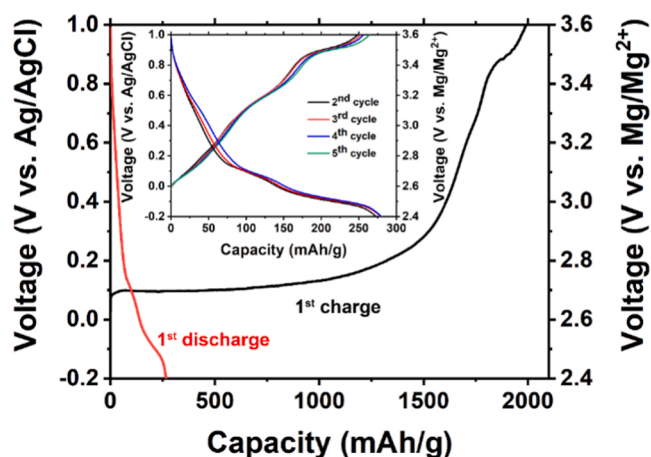


Fig. 2. Performance curves of the first and subsequent four charge-discharge cycles (inset) of the spherical γ -MnS. The electrochemical conversion was carried out in 1 M $\text{Mg}(\text{NO}_3)_2$ aqueous solution at a rate of 50 mA/g.

spectrometer with Rh X-ray source. The electrodes were directly loaded on the sample holder for testing.

X-ray photoelectron spectroscopy (XPS) analysis was performed using a Kratos Axis ULTRA with an Al $K\alpha$ X-ray source. The data processing and peak fitting were performed using the CasaXPS software. The peak position and full width half maximum (FWHM) were analyzed.

Inductively coupled plasma mass spectroscopy (ICP-MS) analysis was performed on a PerkinElmer NexION 350D system. The sample was prepared by scratching off around 2 mg of the cathode materials from electrodes for analysis.

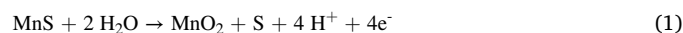
3. Results and discussion

3.1. Preparation of birnessite MnO_2 nanoflowers

Birnessite MnO_2 nanoflowers were prepared using γ -MnS particles as the starting materials through an electrochemical conversion process. The γ -MnS particles were synthesized by a hydrothermal method. SEM study indicates the morphology of γ -MnS particles is spherical with diameters ranging from 200 nm to 2 μm (Fig. 1a). Powder XRD pattern showed the diffraction peaks matched well with those from γ -MnS (PDF#: 00-040-1289) and the final product was in pure hexagonal phase in P63mc space group (Fig. 1b). The conversion to birnessite MnO_2 was carried out by galvanostatically cycling the γ -MnS spheres in 1 M $\text{Mg}(\text{NO}_3)_2$ aqueous solution. Fig. 2 shows the capacity profile of

initial five charge-discharge cycles using γ -MnS nanoparticle as the cathode from -0.2 – 1.0 V (vs. Ag/AgCl) at a rate of 50 mA/g. The long plateau at ~ 0.1 V in the first charge suggests that the conversion reaction of γ -MnS took place during this process and Mn^{2+} ions in γ -MnS were oxidized to Mn^{4+} in MnO_2 . Four more galvanostatical cycles were conducted to complete this conversion reaction. The capacities in the 2nd to 5th cycle were significantly lower than the initial charge process, indicating most of the γ -MnS reacted in the first cycle. After five cycles, the discharge capacity eventually stabilized at ~ 270 mAh/g, suggesting that the conversion was completed (inset of Fig. 2).

Fig. 3a shows the SEM image of the final product after the 5th discharge, showing the transformation of initial spherical particles into flower-like 3D nanostructures. The MnO_2 cathode materials prepared through the electrochemical method show more accessible 3D structures and thinner layers than those made using hydrothermal method (Fig. S1). The HAADF-STEM image depicts there existed the multidomains at few nanometer-sized range. These domains whose boundaries are indicated by the blue lines have different orientations in the nanoflowers (Fig. 3b). The nanocrystalline nature is further supported by the ring pattern observed in the selected area electron diffraction (SAED) image (Fig. S2). STEM-EDS was used to analyze the elemental distribution of this flower-like product. Fig. 3c shows that Mn, O and Mg were evenly distributed in the product, and no S element was detected. The atomic ratio between Mn and O was determined to be approximately 1:2, suggesting the composition of this flower-like material is MnO_2 (Fig. S3, Table S1). Sulfur element, however, was detected to be ~ 19 at% by SEM-EDS and ~ 60 at% by EDXRF on the cathodic electrode (Fig. S4, Table S2 and S3). The content of S detected was relatively high by EDXRF, because EDXRF has a larger penetration depth (~ 100 μm) than SEM-EDS (≤ 2 μm). This result suggests that a separate S-enriched layer was formed besides the nanoflower-like MnO_2 materials after the cycling. XRD pattern of cathode electrode shows sharp diffraction peaks from elemental S besides birnessite MnO_2 (Fig. S5), suggesting the electrochemical process could undergo the following conversion:



Carbon disulfide (CS_2) was used as a solvent to remove the S layer generated because of its good solubility of elemental S. Fig. 3d shows the XRD pattern of the cathode materials after the 5th charge and washing with CS_2 for 2 h. While the diffraction peaks from birnessite MnO_2 remained the same, those from elemental S disappeared [52]. SEM-EDS result shows only 2 at% of S was detected from the final product after the washing step, indicating that S was mostly removed (Fig. S6, Table S4). ICP-MS result shows that the cathode material contains 28.5 wt% of Mn, corresponding to ~ 45 wt% of MnO_2 . The amount of Mg was measured to be 0.58 wt% after the sample charged, and the

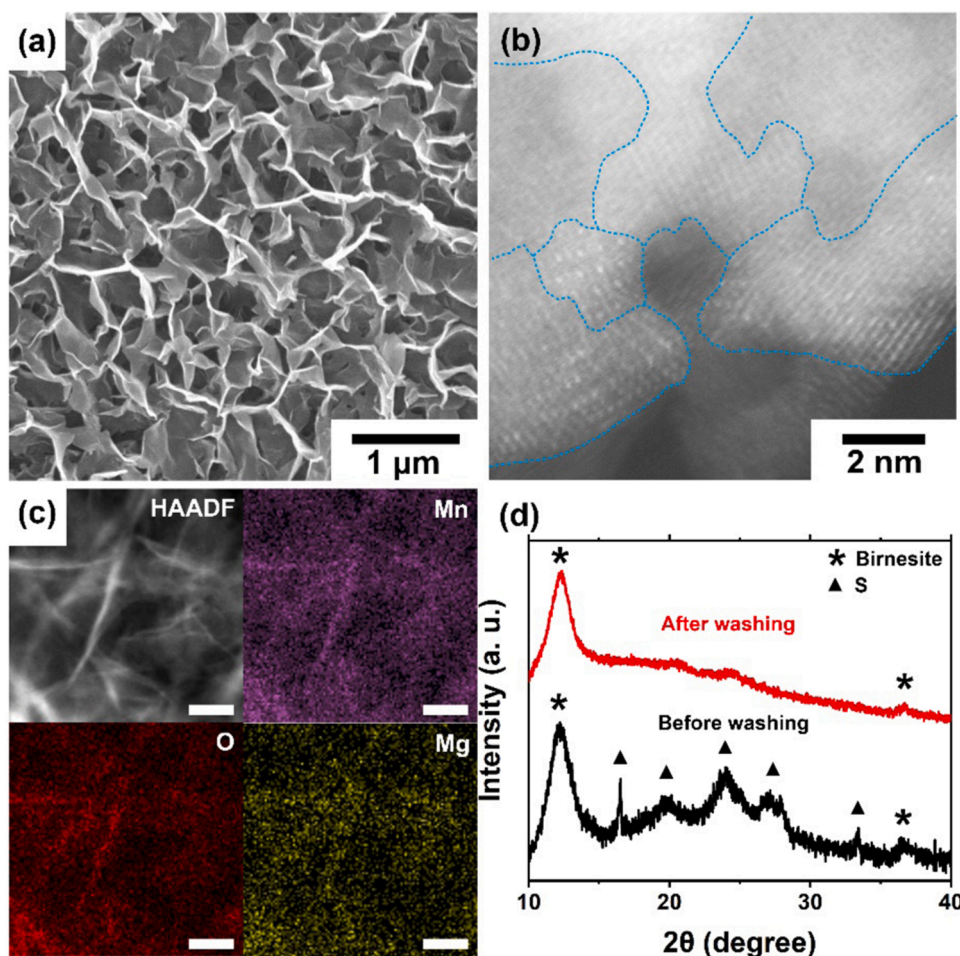


Fig. 3. (a) SEM image, (b) HAADF-STEM image, (c) STEM-EDS mapping of flower-like cathode materials after 5th discharge before CS_2 washing. All scale bars are 50 nm. (d) XRD patterns of the cathode materials obtained after 5th charge before and after washing with CS_2 .

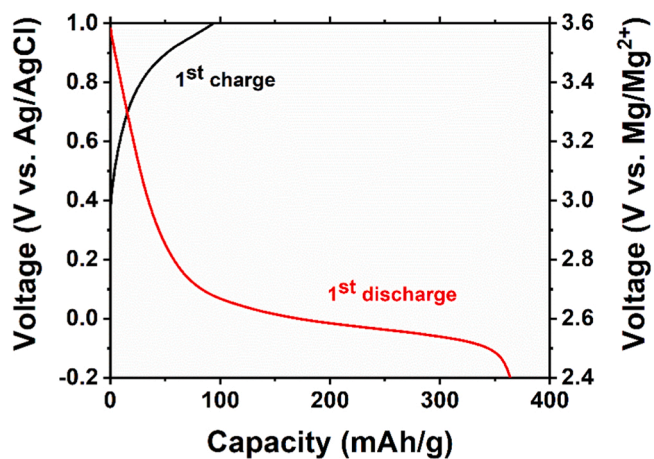


Fig. 4. Representative charge-discharge profile of the birnessite MnO_2 cathode material.

remaining 55 wt% was made of carbon and PVDF (Table S5). This mass ratio of MnO_2 was used for the calculation of mass capacity. Fig. S7 shows that the flower-like morphology remained after the removal of S element, suggesting a good morphological stability of birnessite MnO_2 .

3.2. Electrochemical performance of birnessite MnO_2 nanoflowers

Fig. 4 shows the charge-discharge profile of the birnessite MnO_2 nanoflowers in a 1 M $\text{Mg}(\text{NO}_3)_2$ aqueous electrolyte at a rate of 2 C (616 mA/g). In the first discharge, the voltage decreased rapidly with capacity when the potential was above 0.1 V. This discharge behavior is largely associated with the double layer capacitance [53]. A broad plateau appeared at about 0 V, corresponding to the intercalation of Mg^{2+} ions, which contributed a high capacity of ~ 250 mAh/g. The overall capacity for the first discharge reached around 360 mAh/g. This value is higher than the theoretical capacity of 308 mAh/g for the intercalation of Mg^{2+} into MnO_2 , suggesting surface capacitance contributing to the total appearance capacitance, similar to other metal oxide cathode materials previously reported [54]. The high capacity could be attributed to both high efficiency in ion intercalation and high surface capacitance because of the unique structures of the flower-like morphology made of nm-thin plates. The shortened diffusion depth of the thin layers help facilitate the intercalation of Mg^{2+} ions. Highly accessible surface offered by the open structure provides a large number of active sites for the adsorption of Mg^{2+} ions on the surface of the cathode materials. We further noted that the capacity contributed from both surface capacitance and intercalation increased when the rates decreased (Fig. S8). Furthermore, the discharge capacity changed from ~ 360 mAh/g to ~ 200 mAh/g after ten cycles, likely resulting from the dissolution of Mn (Fig. S9) [33].

Full cell test was conducted using a carbon electrode as the anode and birnessite MnO_2 nanoflowers as the cathode at a rate of 1 C

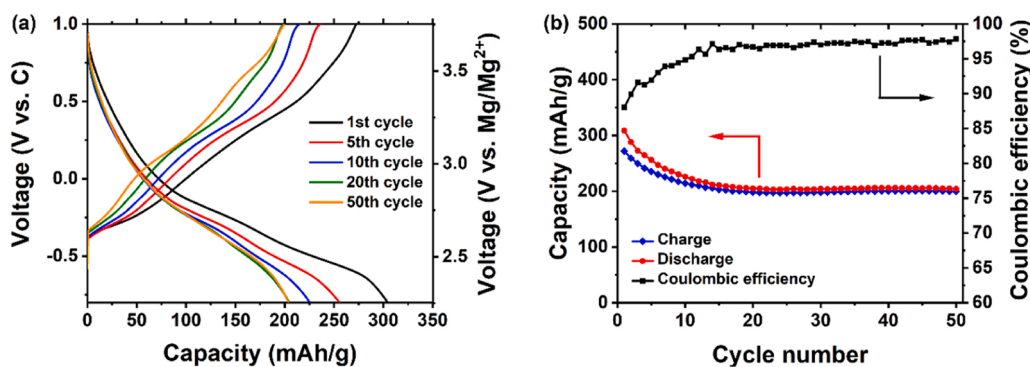


Fig. 5. Performance of full cell tests at a rate of 1 C. (a) Charge-discharge curves of the 1st, 5th, 10th, 20th, and 50th cycle. (b) Charge/discharge capacity and Coulombic efficiency in the first 50 cycles.

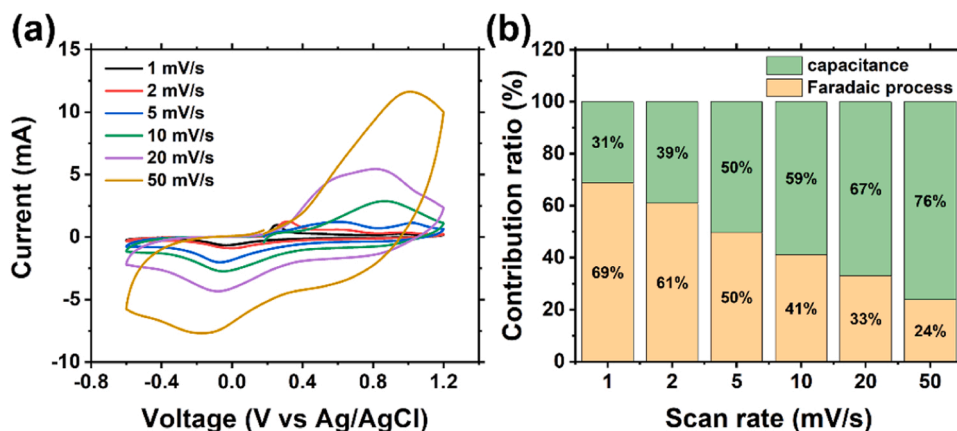


Fig. 6. (a) CV curves and (b) the corresponding contributions of charge storage in MnO₂ from capacitance and Faradaic processes at different scan rates.

(308 mA/g). Fig. 5a shows the charge-discharge curves of the 1st, 5th, 10th, 20th and 50th cycle. The discharge capacity is 309 mAh/g in the initial cycle. The charge-discharge capacity became ~200 mAh/g in the first 20 cycles, and it did not change much in the remaining tests (50 cycles in total). The charge/discharge capacity and the corresponding Coulombic efficiency were presented in Fig. 5b. Both charge and discharge capacity decreased in the first 20 cycles to ~200 mAh/g and stabilized around this value. In the first 20 cycles, the discharge capacity was higher than that for the charge process, leading to low Coulombic efficiency. The Coulombic efficiency increased from ~88% to ~98% after 20 cycles. This conditioning process is similar to what we previously observed for λ -MnO₂ in aqueous electrolyte. [32] The capacity decay and lowered Coulombic efficiency in the initial cycles could be resulted from heterogeneity in local structure and lattice distortion during cycling, as well as the likely side reactions, such as Mn dissolution.

CV study was performed on the final, CS₂-washed birnessite MnO₂ nanoflowers. The scan rate was varied from 1 to 50 mV/s in order to examine the contributions of the Faradaic process and double layer capacitance, respectively, to the overall capacity (Fig. 6). The oxidation peak centered at 0.8 V and the reduction peak was around -0.2 V (Fig. 6a). The contributions of Faradaic process and surface capacitance to the total currents (i) at difference scan rate (v) were quantified by the following equation:

$$i(V) = a_1 v + a_2 v^{0.5} \quad (1)$$

where a_1 and a_2 are the parameters and as functions of operating potential. The two terms on the right-hand side of the equation represent the currents from the double layer capacitance and Faradaic process, respectively. This equation can be rewritten as:

$$\frac{i}{v^{0.5}} = a_1 v^{0.5} + a_2 \quad (2)$$

Thus, a_1 and a_2 can be obtained from a linear fit of $i/v^{0.5}$ as a function of $v^{0.5}$ based on the values obtained from the CV curves at different scan rates (Table S6 and S7). Fig. S10 shows the current contributed from double layer capacitance and Faradaic process at each scan rate.

The shape of CV curves for the Faradaic process remained largely the same, and the reduction peak was around 0 V, which is consistent with the potential of intercalation plateau in the first discharge (Fig. 4). The capacitance increased as the scan rate increased, judging by the area under the CV curves. This result indicates that capacitive response dominated at high scan rates. The contributions from Faradaic process and surface capacitance to the total charge storage were calculated from the areas of CV curves. Fig. 6b shows the contribution from surface capacitance increased from 31% to 76% when the scan rate increased from 1 mV/s to 50 mV/s. These data suggest that capacitance dominated at high scan rates and was more significant in birnessite MnO₂ nanoflowers than others. For example, for 80-nm spinel MnO₂ nanoparticles, double layer capacitance contributed ~17% of the total capacity at a scan rate of 10 mV/s [32], but ~59% for birnessite MnO₂ nanoflowers at the same scan rate. The contribution from capacitive response to the total capacity could be attributed to the large surface area associated with the 3D nanoflower morphology and the crystal phase. Intercalation was dominant at relatively slow scan rates in CV and charge/discharge cycles, in good agreement with the observation of a long discharge plateau, as shown in Fig. 4.

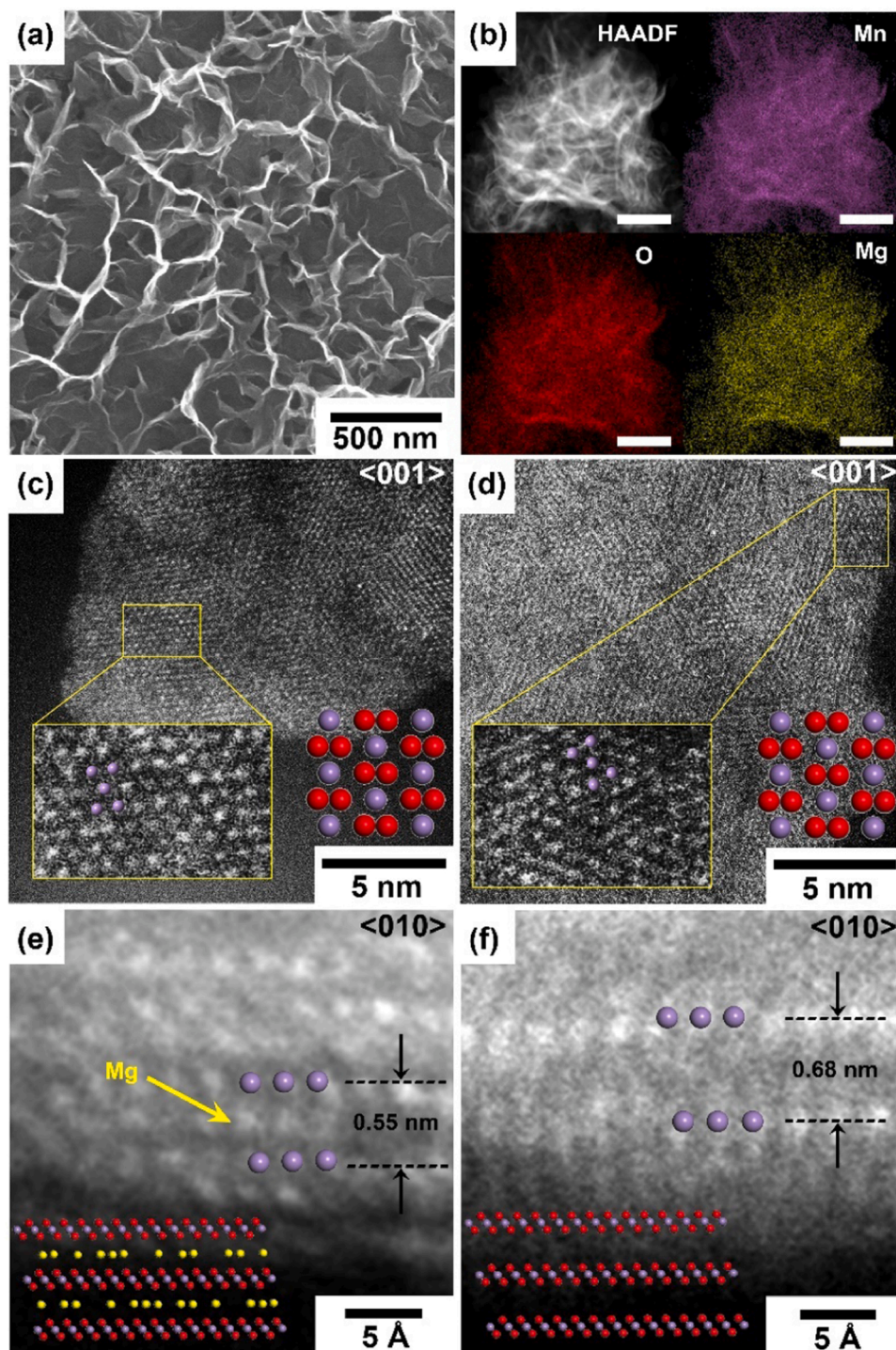


Fig. 7. (a) SEM image, (b) STEM-EDS mapping of birnessite MnO_2 after the first discharge (scale bars: 200 nm). Atomic structure along the (c, d) $\langle 001 \rangle$ and (e, f) $\langle 010 \rangle$ zone axis of birnessite MnO_2 after (c, e) discharge and (d, f) charge. Color code for the illustrations: Mn (purple), O (red), and Mg (yellow).

3.3. Microscopic analysis of the insertion of Mg^{2+}

Fig. 7 shows the electron microscopic studies of birnessite MnO_2 nanoflowers after the first charge and discharge. Representative SEM image shows that the flower-like morphology with 3D open structures well remained after the first cycle (Fig. 7a). STEM-EDS mapping shows the distributions of Mn, O and Mg elements were uniform across the particle of nanoflower after the discharge (Fig. 7b). The atomic ratio between Mn and O remained around 1:2, and a high amount of Mg ($\sim 10\%$) was detected in the active materials, corresponding to an

amount of 0.31 Mg^{2+} per unit formula of MnO_2 , which is equivalent to a capacity of $\sim 190 \text{ mAh/g}$ if the divalent ions intercalated in the solid matrix (Fig. S11, Table S8). HRTEM micrographs show various domains of lattices existed in these MnO_2 nanoflowers after charge and discharge and oriented in different directions (Fig. S12, S13). The domains of these nanoflowers are all a few nanometers in size and exist with rich boundaries between them in the samples after discharge (Fig. S12a-b) and charge stages (Fig. S13a-b), suggesting facile transports should be structurally favored. The SAED contains ring-like patterns with uneven intensities at different angles, indicating the birnessite MnO_2

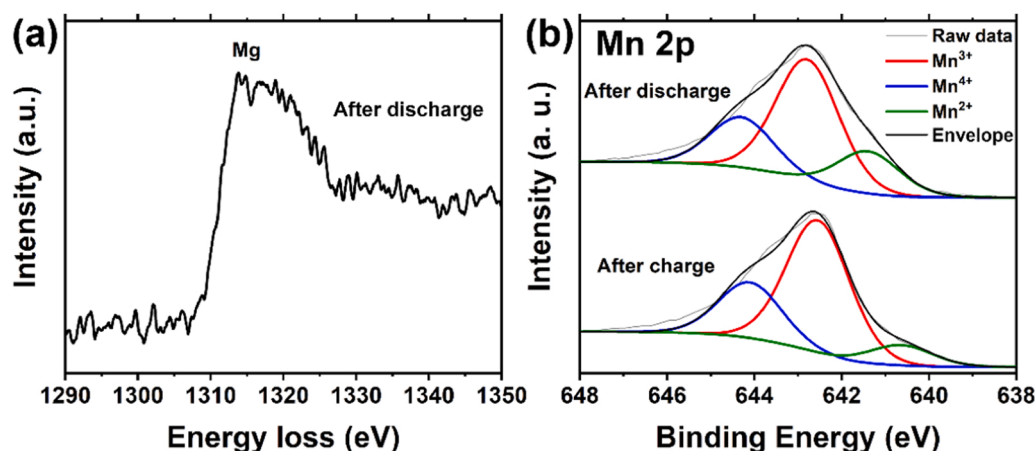


Fig. 8. (a) EELS spectroscopy of Mg K-edge and (b) XPS spectroscopy of Mn 2p region of the birnessite MnO₂ nanoflower cathode after the charge-discharge cycle.

nanoflowers were polycrystalline with many small domains at different orientations (Fig. S12c and S13c). Careful examination of the SAED patterns show the diffraction rings of the discharge samples, shown in Fig. S12c, are brighter than those after charging (Fig. S13c), further indicating the MnO₂ nanoflowers had higher crystallinity after discharge than those after charge.

HAADF-STEM was used to examine the atomic details of the MnO₂ nanoflower cathode materials after the charge-discharge cycle (Fig. 7c-f). Manganese atoms were observed in the STEM images of the layered structures taken along the <001> zone axis because of their large Z contrast (Fig. 7c-d). The Mg atoms were partially blocked by Mn along the <001> zone axis, thus could not be resolved, so there is almost no difference between the STEM images after discharge and charge in Fig. 7c and d. The nanometer-scale contrast variations indicate slightly different orientations in the layered structures, typically < ~3–4 nm in size. Within each domain, lattices exhibit good structural order with the bright spots being Mn atoms. Insertion of Mg²⁺ ions occurred and were observed along the <010> zone axis of the birnessite-type structures (Fig. 7e-f). The bright spots of Mg²⁺ ions were visible between the MnO₂ atomic layers after discharge, which had an average interlayer distance of about 5.5 Å along the <010> zone axis (Fig. 7e). After the charge, no bright spots were observed in between the birnessite MnO₂ layers and the interlayer distance increased to around 6.8 Å (Fig. 7f). The average layer spacing of 6.8 Å for the charged sample agrees well with that previously reported (7 Å) [33]. This change in interlayer spacing could be understood because after the discharge, Mg²⁺ ion inserted into the layer space of MnO₂ host structures with oxygen anions in contact with the guest cations, and the charge interaction pulled the exposed oxygen anions closer [33,55]. Up to ~10 at% Mg was detected in the discharged sample and 2.6 at% Mg was detected after the first charge by STEM-EDS (Table S8 and S9). The fine nm-sized domain size and layered nature of nanoflowers could greatly facilitate the interaction of Mg²⁺ ions, especially at a large number of edges of layered structures along the <010> direction of birnessite MnO₂.

3.4. EELS and XPS characterizations

EELS and XPS were carried out to further study the chemical environment of birnessite MnO₂ and Mg²⁺ ions in the host structures after the charge and discharge stages. Fig. 8a shows the EELS spectroscopy of Mg K-edge in birnessite MnO₂ nanoflowers after the first discharge. The peak with an onset edge energy of around 1310 eV indicates there exists a large amount of Mg²⁺ ions within the probed area (Fig. S14). The value of onset energy for Mg²⁺ ions was shown to be 10 eV higher than that of Mg metal in the EELS. Both the onset energy and the observed Mg edge fine structure were in agreement with those of the Mg²⁺ ions shown in the previous study [56]. The XPS Mg 1s spectra, which were taken from

a much larger volume than that in EELS, show that the oxidation state of Mg cations did not change greatly between the charge and discharge samples, suggesting only Mg²⁺ ions were involved and no reduced Mg species formed (Fig. S15a). The XPS data show the overall oxidation state of Mn cations in these nanoflowers decreased after the discharge (Fig. 8b, Table S10). After the charge, Mn³⁺/Mn⁴⁺ ratio dropped when compared to that after the discharge, as measured by the peak areas. This result suggests that Mg²⁺ ions intercalated into MnO₂ in the discharge, resulting in a drop in the average oxidation state of Mn cations (Table S10). The XPS O 1s data whose peaks centered at 530 eV with a shoulder at 532 eV, which can be assigned to hydroxide or oxyhydroxide group, could result from the formation of MnOOH (Fig. S15b) [33]. EELS spectroscopy was used to examine the surface oxidation state of the birnessite MnO₂ nanoflowers (Fig. S16). Specifically, the Mn L_{2,3} ratio was used to evaluate the oxidation state of Mn [57,58]. Our results show that this ratio is similar between the samples after charge and discharge. This observation is likely associated with the formation of a MnO_x shell on the surface of birnessite MnO₂ after the galvanostatic cycles in an aqueous electrolyte. Similar phenomenon was reported previously in aqueous electrolytes with both λ-MnO₂ and α-MnO₂ [59, 60]. Thus, the formation of MnO_x shell renders it impossible using EELS to detect the changes in electronic configuration of the bulk in these materials.

4. Conclusions

We developed an approach to the preparation of birnessite MnO₂ nanoflowers from γ-MnS spheres through an unconventional, electrochemical process. These MnO₂ nanoflowers with fine nm-sized domains were used as cathode materials for Mg²⁺ intercalation, exhibiting a capacity of up to about 360 mAh/g in the initial discharge in aqueous electrolyte. In the full cell tests using a carbon electrode as the anode, an initial discharge capacity was measured to be 309 mAh/g and the charge-discharge capacity became and maintained at ~200 mAh/g for 50 cycles. STEM-HAADF studies provide direct evidence for the intercalation of Mg²⁺ ions in the atomic layers of MnO₂ nanoflowers. This result highlights an important benefit of using nm-sized, open structures as electrode materials. Thus, this study provides a viable and facile strategy in the design of electrode materials for multivalent ion batteries based on unique, ion-accessible 3D nanostructures.

CRediT authorship contribution statement

Cheng Zhang: Conceptualization, Methodology, Writing - original draft, Writing - review & editing, Data curation, Validation, Formal analysis, Investigation. **Xun Zhan:** Data curation, Methodology. **Talha Al-Zoubi:** Data curation, Methodology. **Yangling Ma:** Data curation,

Methodology. **Pei-Chieh Shih:** Data curation, Methodology. **Fangfang Wang:** Data curation. **Wenxiang Chen:** Data curation. **Saran Pidaparthi:** Data curation. **Ryan M. Stephens:** Supervision, Conceptualization, Investigation, Resources. **Qian Chen:** Supervision, Conceptualization, Investigation, Resources, Funding acquisition. **Jian-Min Zuo:** Supervision, Conceptualization, Investigation, Resources, Funding acquisition. **Hong Yang:** Supervision, Conceptualization, Investigation, Resources, Funding acquisition, Writing - review & editing.

Declaration of Competing Interest

The authors declare that they have no known competing financial interests or personal relationships that could have appeared to influence the work reported in this paper.

Data availability

Data will be made available on request.

Acknowledgments

This work is supported in part by the Energy & Biosciences Institute through the EBI-Shell program. Y. M. and F. W. thank a scholarship from China Scholarship Council (CSC). Electron microscopy characterizations were carried out at the Frederick Seitz Materials Research Laboratory Central Research Facilities, University of Illinois. The X-ray diffraction was carried out at the George L. Clark X-ray Facility and 3 M Materials Laboratory, School of Chemical Science at University of Illinois at Urbana-Champaign.

Appendix A. Supporting information

Supplementary data associated with this article can be found in the online version at [doi:10.1016/j.nanoen.2022.107696](https://doi.org/10.1016/j.nanoen.2022.107696).

References

- P. Canepa, G. Sai Gautam, D.C. Hannah, R. Malik, M. Liu, K.G. Gallagher, K. A. Persson, G. Ceder, Odyssey of multivalent cathode materials: open questions and future challenges, *Chem. Rev.* 117 (2017) 4287–4341.
- M.M. Huie, D.C. Bock, E.S. Takeuchi, A.C. Marschilok, K.J. Takeuchi, Cathode materials for magnesium and magnesium-ion based batteries, *Coord. Chem. Rev.* 287 (2015) 15–27.
- J. Muldoon, C.B. Bucur, T. Gregory, Ferrous hype behind magnesium batteries: an open call to synthetic chemists-electrolytes and cathodes needed, *Angew. Chem. Int. Ed.* 56 (2017) 12064–12084.
- J. Song, E. Sahadeo, M. Noked, S.B. Lee, Mapping the challenges of magnesium battery, *J. Phys. Chem. Lett.* 7 (2016) 1736–1749.
- A. Ponrouch, J. Bitenc, R. Dominko, N. Lindahl, P. Johansson, M.R. Palacin, Multivalent rechargeable batteries, *Energy Storage Mater.* 20 (2019) 253–262.
- G.Z. Fang, J. Zhou, A.Q. Pan, S.Q. Liang, Recent advances in aqueous zinc-ion batteries, *ACS Energy Lett.* 3 (2018) 2480–2501.
- D. Selvakumaran, A.Q. Pan, S.Q. Liang, G.Z. Cao, A review on recent developments and challenges of cathode materials for rechargeable aqueous Zn-ion batteries, *J. Mater. Chem. A* 7 (2019) 18209–18236.
- S.K. Das, S. Mahapatra, H. Lahan, Aluminium-ion batteries: developments and challenges, *J. Mater. Chem. A* 5 (2017) 6347–6367.
- H. Wang, X.F. Feng, Y. Chen, Y.S. Liu, K.S. Han, M.X. Zhou, M.H. Engelhard, V. Murugesan, R.S. Assary, T.L. Liu, W. Henderson, Z.M. Nie, M. Gu, J. Xiao, C. M. Wang, K. Persson, D.H. Mei, J.G. Zhang, K.T. Mueller, J.H. Guo, K. Zavadil, Y. Y. Shao, J. Liu, Reversible electrochemical interface of Mg metal and conventional electrolyte enabled by intermediate adsorption, *ACS Energy Lett.* 5 (2020) 200–206.
- H.Y. Asl, A. Manthiram, Mass transfer of divalent ions in an oxide host: comparison of Mg^{2+} and Zn^{2+} diffusion in hexagonal $K_xW_3O_9$ bronze, *Chem. Mater.* 31 (2019) 2296–2307.
- L.E. Blanc, X.Q. Sun, A. Shyamsunder, V. Duffort, L.F. Nazar, Direct nano-synthesis methods notably benefit Mg-battery cathode performance, *Small Methods* 4 (2020), 2000029.
- K. Ta, K.A. See, A.A. Gewirth, Elucidating Zn and Mg electrodeposition mechanisms in nonaqueous electrolytes for next-generation metal batteries, *J. Phys. Chem. C* 122 (2018) 13790–13796.
- M. Li, J. Lu, X.L. Ji, Y.G. Li, Y.Y. Shao, Z.W. Chen, C. Zhong, K. Amine, Design strategies for nonaqueous multivalent-ion and monovalent-ion battery anodes, *Nat. Rev. Mater.* 5 (2020) 276–294.
- J. Zhang, Z. Chang, Z. Zhang, A. Du, S. Dong, Z. Li, G. Li, G. Cui, Current design strategies for rechargeable magnesium-based batteries, *ACS Nano* 15 (2021) 15594–15624.
- S. Hou, X. Ji, K. Gaskell, P.-F. Wang, L. Wang, J. Xu, R. Sun, O. Borodin, C. Wang, Solvation sheath reorganization enables divalent metal batteries with fast interfacial charge transfer kinetics, *Science* 374 (2021) 172–178.
- Y.Y. Liu, Y.Y. Zhu, Y. Cui, Challenges and opportunities towards fast-charging battery materials, *Nat. Energy* 4 (2019) 540–550.
- E.R. Logan, J.R. Dahn, Electrolyte design for fast-charging Li-ion batteries, *Trends Chem.* 2 (2020) 354–366.
- J.B. Goodenough, K.S. Park, The Li-ion rechargeable battery: a perspective, *J. Am. Chem. Soc.* 135 (2013) 1167–1176.
- C.F. Liu, Z.G. Neale, G.Z. Cao, Understanding electrochemical potentials of cathode materials in rechargeable batteries, *Mater. Today* 19 (2016) 109–123.
- D.C. Lin, Y.Y. Liu, Y. Cui, Reviving the lithium metal anode for high-energy batteries, *Nat. Nanotechnol.* 12 (2017) 194–206.
- H. Li, Z.X. Wang, L.Q. Chen, X.J. Huang, Research on advanced materials for Li-ion batteries, *Adv. Mater.* 21 (2009) 4593–4607.
- K. Liu, Y.Y. Liu, D.C. Lin, A. Pei, Y. Cui, Materials for lithium-ion battery safety, *Sci. Adv.* 4 (2018) 9820.
- N. Nitta, F.X. Wu, J.T. Lee, G. Yushin, Li-ion battery materials: present and future, *Mater. Today* 18 (2015) 252–264.
- B.L. Mehdi, J. Qian, E. Nasybulin, C. Park, D.A. Welch, R. Faller, H. Mehta, W. A. Henderson, W. Xu, C.M. Wang, J.E. Evans, J. Liu, J.G. Zhang, K.T. Mueller, N. D. Browning, Observation and quantification of nanoscale processes in lithium batteries by operando electrochemical (S)TEM, *Nano Lett.* 15 (2015) 2168–2173.
- M.L. Mao, T. Gao, S.Y. Hou, C.S. Wang, A critical review of cathodes for rechargeable Mg batteries, *Chem. Soc. Rev.* 47 (2018) 8804–8841.
- Y.Y. Liu, G.J. He, H. Jiang, I.P. Parkin, P.R. Shearing, D.J.L. Brett, Cathode design for aqueous rechargeable multivalent ion batteries: challenges and opportunities, *Adv. Funct. Mater.* 31 (2021), 2010445.
- D. Aurbach, Z. Lu, A. Schechter, Y. Gofer, H. Gizbar, R. Turgeman, Y. Cohen, M. Moshkovich, E. Levi, Prototype systems for rechargeable magnesium batteries, *Nature* 407 (2000) 724–727.
- L.W.F. Wan, B.R. Perdue, C.A. Appleby, D. Prendergast, Mg desolvation and intercalation mechanism at the Mg_6S_8 Chevrel phase surface, *Chem. Mater.* 27 (2015) 5932–5940.
- L. Mei, J.T. Xu, Z.X. Wei, H.K. Liu, Y.T. Li, J.M. Ma, S.X. Dou, Chevrel phase Mg_6T_3 ($T = S, Se$) as electrodes for advanced energy storage, *Small* 13 (2017), 1801441.
- R.G. Zhang, X.Q. Yu, K.W. Nam, C. Ling, T.S. Arthur, W. Song, A.M. Knapp, S. N. Ehrlich, X.Q. Yang, M. Matsui, α - MnO_2 as a cathode material for rechargeable Mg batteries, *Electrochem. Commun.* 23 (2012) 110–113.
- C. Kim, P.J. Phillips, B. Key, T. Yi, D. Nordlund, Y.S. Yu, R.D. Bayliss, S.D. Han, M. He, Z. Zhang, A.K. Burrell, R.F. Klie, J. Cabana, Direct observation of reversible magnesium ion intercalation into a spinel oxide host, *Adv. Mater.* 27 (2015) 3377–3384.
- W. Chen, X. Zhan, B. Luo, Z. Ou, P.C. Shih, L. Yao, S. Pidaparthi, A. Patra, H. An, P. V. Braun, R.M. Stephens, H. Yang, J.M. Zuo, Q. Chen, Effects of particle size on Mg^{2+} ion intercalation into λ - MnO_2 cathode materials, *Nano Lett.* 19 (2019) 4712–4720.
- X. Sun, V. Duffort, B.L. Mehdi, N.D. Browning, L.F. Nazar, Investigation of the mechanism of Mg insertion in birnessite in nonaqueous and aqueous rechargeable Mg-ion batteries, *Chem. Mater.* 28 (2016) 534–542.
- B. Jia, W. Chen, J. Luo, Z. Yang, L. Li, L. Guo, Construction of MnO_2 artificial leaf with atomic thickness as highly stable battery anodes, *Adv. Mater.* 32 (2020), 1906582.
- A. Boisset, L. Athouel, J. Jacquemin, P. Porion, T. Brousse, M. Anouti, Comparative performances of birnessite and cryptomelane MnO_2 as electrode material in neutral aqueous lithium salt for supercapacitor application, *J. Phys. Chem. C* 117 (2013) 7408–7422.
- S. Kim, K.W. Nam, S. Lee, W. Cho, J.S. Kim, B.G. Kim, Y. Oshima, J.S. Kim, S. G. Doo, H. Chang, D. Aurbach, J.W. Choi, Direct observation of an anomalous spinel-to-layered phase transition mediated by crystal water intercalation, *Angew. Chem. Int. Ed.* 54 (2015) 15094–15099.
- S. Kim, S. Lee, K.W. Nam, J. Shin, S.Y. Lim, W. Cho, K. Suzuki, Y. Oshima, M. Hirayama, R. Kanno, J.W. Choi, On the mechanism of crystal water insertion during anomalous spinel-to-birnessite phase transition, *Chem. Mater.* 28 (2016) 5488–5494.
- K.W. Nam, S. Kim, S. Lee, M. Salama, I. Shterenberg, Y. Gofer, J.S. Kim, E. Yang, C. S. Park, J.S. Kim, S.S. Lee, W.S. Chang, S.G. Doo, Y.N. Jo, Y. Jung, D. Aurbach, J. W. Choi, The high performance of crystal water containing manganese birnessite cathodes for magnesium batteries, *Nano Lett.* 15 (2015) 4071–4079.
- C. Ling, R.G. Zhang, T.S. Arthur, F. Mizuno, How general is the conversion reaction in Mg battery cathode: a case study of the magnesiation of α - MnO_2 , *Chem. Mater.* 27 (2015) 5799–5807.
- F. Tuerxun, S. Otani, K. Yamamoto, T. Matsunaga, H. Imai, T. Mandai, T. Watanabe, T. Uchiyama, K. Kanamura, Y. Uchimoto, Phase transition behavior of $MgMn_2O_4$ spinel oxide cathode during magnesium ion insertion, *Chem. Mater.* 33 (2021) 1006–1012.
- T. Hatakeyama, H. Li, N.L. Okamoto, K. Shimokawa, T. Kawaguchi, H. Tanimura, S. Hirayama, M. Fichtner, T. Ichitsubo, Accelerated kinetics revealing metastable pathways of magnesiation-induced transformations in MnO_2 polymorphs, *Chem. Mater.* 33 (2021) 6983–6996.

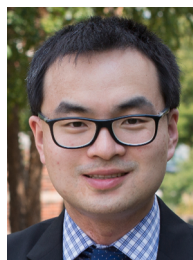
- [42] X. Guo, S. Yang, D. Wang, A. Chen, Y. Wang, P. Li, G. Liang, C. Zhi, The energy storage mechanisms of MnO_2 in batteries, *Curr. Opin. Electrochem.* 30 (2021), 100769.
- [43] Y. Xu, Z.C. Liu, X.H. Zheng, K. Li, M.M. Wang, W. Yu, H.L. Hu, W. Chen, Solid electrolyte interface regulated by solvent-in-water electrolyte enables high-voltage and stable aqueous Mg- MnO_2 batteries, *Adv. Energy Mater.* (2022).
- [44] L. Han, J.F. Li, X.L. Zhang, H.L. Huang, Z.L. Yang, G. Zhu, M. Xu, L.K. Pan, Low-crystalline akhtenskite MnO_2 -based aqueous magnesium-ion hybrid supercapacitors with a superior energy density boosted by redox bromide-ion additive electrolytes, *ACS Sustain. Chem. Eng.* 9 (2021) 9165–9176.
- [45] X.Q. Sun, P. Bonnicks, V. Duffort, M. Liu, Z.Q. Rong, K.A. Persson, G. Ceder, L. F. Nazar, A high capacity thiospinel cathode for Mg batteries, *Energy Environ. Sci.* 9 (2016) 2273–2277.
- [46] Y. Orikasa, T. Masese, Y. Koyama, T. Mori, M. Hattori, K. Yamamoto, T. Okado, Z. D. Huang, T. Minato, C. Tassel, J. Kim, Y. Kobayashi, T. Abe, H. Kageyama, Y. Uchimoto, High energy density rechargeable magnesium battery using earth-abundant and non-toxic elements, *Sci. Rep.* 4 (2014) 5622.
- [47] J.L. Andrews, A. Mukherjee, H.D. Yoo, A. Parija, P.M. Marley, S. Fakra, D. Prendergast, J. Cabana, R.F. Klie, S. Banerjee, Reversible Mg-ion insertion in a metastable one-dimensional polymorph of V_2O_5 , *Chem* 4 (2018) 564–585.
- [48] T.S. Arthur, K. Kato, J. Germain, J.H. Guo, P.A. Glans, Y.S. Liu, D. Holmes, X. D. Fan, F. Mizuno, Amorphous $\text{V}_2\text{O}_5\text{-P}_2\text{O}_5$ as high-voltage cathodes for magnesium batteries, *Chem. Commun.* 51 (2015) 15657–15660.
- [49] Z.Z. Liu, X. Li, J. He, Q. Wang, D. Zhu, Y.G. Yan, Y.G. Chen, Is proton a charge carrier for $\delta\text{-MnO}_2$ cathode in aqueous rechargeable magnesium-ion batteries? *J. Energy Chem.* 68 (2022) 572–579.
- [50] W. Lv, J. Meng, Y. Li, W. Yang, Y. Tian, X. Lyu, C. Duan, X. Ma, Y. Wu, Inexpensive and eco-friendly nanostructured birnessite-type $\delta\text{-MnO}_2$: A design strategy from oxygen defect engineering and K^+ pre-intercalation, *Nano Energy* 98 (2022), 107274.
- [51] Q. Xie, G. Cheng, T. Xue, L. Huang, S. Chen, Y. Sun, M. Sun, H. Wang, L. Yu, Alkali ions pre-intercalation of $\delta\text{-MnO}_2$ nanosheets for high-capacity and stable Zn-ion battery, *Mater. Today Energy* 24 (2022), 100934.
- [52] H.M. Chen, J.H. He, C.B. Zhang, H. He, Self-assembly of novel mesoporous manganese oxide nanostructures and their application in oxidative decomposition of formaldehyde, *J. Phys. Chem. C* 111 (2007) 18033–18038.
- [53] A. Noori, M.F. El-Kady, M.S. Rahmanifar, R.B. Kaner, M.F. Mousavi, Towards establishing standard performance metrics for batteries, supercapacitors and beyond, *Chem. Soc. Rev.* 48 (2019) 1272–1341.
- [54] Q. Li, H.S. Li, Q.T. Xia, Z.Q. Hu, Y. Zhu, S.S. Yan, C. Ge, Q.H. Zhang, X.X. Wang, X. T. Shang, S.T. Fan, Y.Z. Long, L. Gu, G.X. Miao, G.H. Yu, J.S. Moosera, Extra storage capacity in transition metal oxide lithium-ion batteries revealed by in situ magnetometry, *Nat. Mater.* 20 (2020) 76–83.
- [55] H. Xia, X.H. Zhu, J.Z. Liu, Q. Liu, S. Lan, Q.H. Zhang, X.Y. Liu, J.K. Seo, T.T. Chen, L. Gu, Y.S. Meng, A monoclinic polymorph of sodium birnessite for ultrafast and ultrastable sodium ion storage, *Nat. Commun.* 9 (2018) 5100.
- [56] T.S. Arthur, P.A. Glans, M. Matsui, R.G. Zhang, B.W. Ma, J.H. Guo, Mg deposition observed by in situ electrochemical Mg K-edge X-ray absorption spectroscopy, *Electrochem. Commun.* 24 (2012) 43–46.
- [57] L. Laffont, P. Gibot, High resolution electron energy loss spectroscopy of manganese oxides: Application to Mn_3O_4 nanoparticles, *Mater. Charact.* 61 (2010) 1268–1273.
- [58] X. Zhan, J.-M. Zuo, W. Chen, Q. Chen, Determination of Mn valences in $\text{Li}_{1-x}\text{Mg}_x\text{Mn}_2\text{O}_4$ using monochromated EELS in an aberration-corrected STEM, *Microsc. Microanal.* 25 (2019) 658–659.
- [59] Q.D. Truong, M.K. Devaraju, P.D. Tran, Y. Gambe, K. Nayuki, Y. Sasaki, I. Honma, Unravelling the surface structure of MgMn_2O_4 cathode materials for rechargeable magnesium-ion battery, *Chem. Mater.* 29 (2017) 6245–6251.
- [60] T.S. Arthur, R.G. Zhang, C. Ling, P.A. Glans, X.D. Fan, J.H. Guo, F. Mizuno, Understanding the electrochemical mechanism of K-alpha MnO_2 for magnesium battery cathodes, *ACS Appl. Mater. Interfaces* 6 (2014) 7004–7008.



Talha Al-Zoubi A Chicago-native Talha went on to receive his B.S. in chemical engineering from the University of Illinois at Chicago in 2016. He immediately went on to join Professor Hong Yang's group at the University of Illinois at Urbana-Champaign. His thesis research has focused on the development and characterization of non-precious metal electrocatalysts for fuel cell applications. Specifically, he has worked on metal-organic framework materials and their utilization as precursors to catalytic materials for the oxygen reduction reaction.



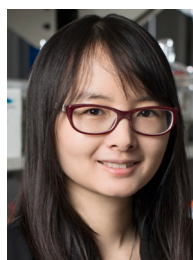
Yanling Ma received her B.S. at University of Science and Technology of Beijing in 2015. She then went to Shanghai Jiao Tong University to pursue her Ph.D under the supervision of Professor Jianbo Wu and Professor Tao Deng in the School of Materials Science and Engineering. She joined Professor Hong Yang's group at the University of Illinois at Urbana-Champaign in 2018 as a visiting scholar. Her doctoral research has focused on the design and characterization of electrocatalysts for fuel cells and in situ TEM characterization of gas phase chemical reactions.



Wenxiang Chen is a post-doctoral research associate in Materials Science and Engineering at University of Illinois Urbana-Champaign since 2017. His research focuses on phase transformation and heterogeneity in ion-insertion solids based on advanced electron microscopy. Previously, he received his Ph. D. in Electrical and Systems Engineering at University of Pennsylvania.



Ryan Stephens is team lead for energy storage in Shell's Power Technology organization. In this role, he has led projects in multiple areas of electrochemical energy storage, including conversion electrodes, solid-state electrolytes, electrode stability and electrolyte structure, and in situ analysis of multi-valent intercalation electrodes. He holds a Ph.D. in chemical engineering from the University of Illinois at Urbana-Champaign.



Qian Chen is an Associate Professor and Racheff Faculty Scholar in Materials Science and Engineering at UIUC. She received her PhD degree in 2012 from the same department and did her postdoctoral training as a Miller Fellow at UC Berkeley. She started her faculty position in UIUC from 2015. She is the winner of Hanwha-TotalEnergies IUPAC Young Polymer Scientist Award, Unilever Award from ACS, Sloan Fellow, US Air Force's YIP, and CAREER Award from US NSF. Her research interests are on the structure, form, and function of soft and energy matter at the nanoscale.



Cheng Zhang graduated from Tsinghua University in 2017 with a bachelor's degree in chemical engineering. Then he joined Professor Hong Yang's group at the University of Illinois at Urbana-Champaign as a Ph.D student. His graduate research has focused on the development of cathode materials for energy storage devices and efficient electrocatalysts for oxygen evolution reaction.



Jian-Min Zuo is Ivan Racheff professor of Materials Science and Engineering at University of Illinois. He received his Ph.D. in Physics from Arizona State University (ASU) in 1989. He then took a three-year postdoctoral fellowship at the National Science Foundation center for high resolution electron microscopy and the Physics department at ASU. He co-authored two books on Electron Microdiffraction and Advanced Transmission Electron Microscopy with John Spence. His research focuses on the advancement of electron diffraction and microscopy and understanding of structure-property relationships in a broad range of materials.



Hong Yang is the Richard C. Alkire Chair in Chemical Engineering at UIUC. He received his PhD degree in 1998 from University of Toronto and did his postdoctoral training as an NSERC Postdoctoral Fellow at Harvard University. He worked at University of Rochester between 2001 and 2011, moved to UIUC in 2012. He is an elected Fellow of AAAS, winner of Doctoral Prize from NSERC Canada, and CAREER Award from US NSF. His research interests are on the material chemistry approach to the development of nanostructures for catalysis, energy, sustainability, and biological applications.